Journal of Cleaner Production 467 (2024) 142912

Contents lists available at ScienceDirect

Journal of Cleaner Production

journal homepage: www.elsevier.com/locate/jclepro

Modelling and energy efficiency analysis of the microwave continuous processing of limestone

Sofia N. Gonçalves [a,*], Duarte M.S. Albuquerque [a,b,c], José C.F. Pereira [a]

[a] IDMEC, Instituto Superior Técnico, Universidade de Lisboa, 1049-001 Lisboa, Portugal
[b] UNIDEMI, Department of Mechanical and Industrial Engineering, NOVA School of Science and Technology, Universidade NOVA de Lisboa, 2829-516, Caparica, Portugal[1]
[c] Laboratório Associado de Sistemas Inteligentes (LASI), 4800-058, Guimarães, Portugal

ARTICLE INFO

Handling Editor: Jin-Kuk Kim

Keywords:
Microwave continuous processing
Very-high temperature microwave heating
Impedance matching control
Multiphysics numerical simulation

ABSTRACT

Our numerical investigation is oriented to the energy efficiency of the microwave heating technology for the continuous production of cement clinker.

Simulations of the novel microwave continuous processing of limestone are performed using the COMSOL Multiphysics® Software. The proposed mathematical model couples Maxwell's equations with energy and chemical equations, and numerical verification and validation are undertaken to support the accuracy of the results in this work. This approach includes automatic control actions regulating energy input and cavity impedance. A rectangular waveguide, operating as a single-mode cavity at 2.45 GHz, is utilized. The impact of various fill ratios of material on the system's efficiency unveiled an intriguing heat transfer mechanism responsible for optimal operational conditions, with microwave efficiency up to 75% and thermal efficiency exceeding 90%. Notably, the potential of microwave technology in reducing greenhouse gas emissions is contingent upon establishing clean energy sources for electricity production.

1. Introduction

To meet the greenhouse gas reduction targets, energy-intensive industries are encouraged to adopt cost-effective and eco-friendly energy solutions. The cement industry, contributing nearly 7% of global CO_2 emissions, is a key sector under scrutiny (Voldsund et al., 2019). In cement production, rotary kilns consume 82% of the available energy, operating at under 40% thermal efficiency and contributing with 90% of the process CO2 emissions (Choate, 2003). There are various opportunities to improve this process, ranging from raising awareness about energy management to investing in upgraded equipment or innovative technologies (Fennell et al., 2022).

For processes operating at lower temperatures, the industrial use of microwave heating (MWH) has been firmly established within the oil and food drying sectors (Zhu et al., 2022; Zaki et al., 2023). Applications of MWH also extend to material processing and curing (Li et al., 2022; Kong et al., 2021). The future competitive edge of MWH over conventional heating (CH) has been attributed to its capability for faster processing, decreased energy consumption, and lower operational costs (Papargyris et al., 2008; Lu et al., 2024). Numerous materials witness improvements in their mechanical and physical characteristics through MWH. This holds true for cement-based materials, where there are enhancements in cementitious properties and expedited strength development observed in Portland cement mortar (Huang et al., 2009; Makul et al., 2014).

For processes requiring extremely high temperatures, there is promising news regarding industry electrification and the potential adoption of continuous microwave technology. Energy-intensive industries have shown encouraging signs of reducing energy consumption by 60% to 80% and lowering 3 to 5 times the CO_2 emissions (Amini et al., 2021). Recent reports highlight successful demonstrations of sintering clinker using MHW, resulting in higher strength and comparable properties to commercially produced clinker, while also reducing sintering time and required temperatures (Kaewwichit et al., 2016). A more recent advancement featured an electrified calciner modelled with resistance-based heating and integrated into an existing kiln system, achieving an impressive 94% calcination degree with substantial net reduction in CO_2 emissions from 114 tonnes per hour to 32 tonnes per hour (Tokheim et al., 2019). Ceralink's Microwave Assist

* Corresponding author.
E-mail addresses: sofia.goncalves@tecnico.ulisboa.pt (S.N. Gonçalves), duartealbuquerque@tecnico.ulisboa.pt (D.M.S. Albuquerque), jcfpereira@tecnico.ulisboa.pt (J.C.F. Pereira).

[1] Present address.

https://doi.org/10.1016/j.jclepro.2024.142912
Received 24 January 2024; Received in revised form 9 May 2024; Accepted 13 June 2024
Available online 18 June 2024

Technology demonstrated accelerated limestone calcination rates while consuming less energy than the conventional method. Assessment of the proposed post-heating design in a traditional calciner and the retrofitting of rotary kiln equipment revealed their feasibility in the lime industry (Esquenazi et al., 2011; Fall et al., 2012).

Greenhouse Gas (GHG) emissions resulting from electricity production and use in Europe have notably decreased in the last three decades, showing varying reductions for EU countries. Between 1990 and 2019, there was a 50% decrease in carbon intensity in the electricity used at low voltage (Scarlat et al., 2022). Europe has introduced the Green Deal as part of its new Growth strategy, responding to one of today's most pressing challenges: climate change. By 2050, Europe aims to achieve climate neutrality while boosting the economy, fostering sustainable industries and transportation. The Green Deal unveiled in 2019 was incorporated into the European Climate Law established in 2021. According to this law, the EU is committed to reducing emissions by 55% by 2030 and has a binding target of achieving net zero greenhouse gas emissions by 2050. To meet these targets and revise and update EU legislation, the European Commission has introduced the Fit for 55 proposal. Among its trends is the increased use of clean energy for electricity production, supporting the electrification of heavy industries and the adoption of microwave technology.

Reliable findings exist regarding the efficiency of microwave-driven processes in handling substantial material loads, yet only 12% of scientific studies record the processing of samples exceeding 200 g (Bermúdeza et al., 2015). While lab-scale temperature profiles are crucial for rapid kinetics, replicating them in a large batch microwave furnace is not so straight forward as the limited penetration of microwaves would require a significant reduction in the microwave frequency (Goyal et al., 2022).

The solution lies in Microwave Continuous Processing Technology (Patil et al., 2014). Demonstrations of large-scale continuous microwave pyrolysis have effectively addressed resource inefficiencies and energy limitations, resulting in innovative solutions for emerging fuels, improved product quality and increased yield (Dadsetan et al., 2023; Juan et al., 2021; Zhou et al., 2023). However, further studies are required to explore other microwave continuous processes, preferably with substantial mass fluxes to achieve scalability and develop larger commercial high-temperature microwave units. In pursuit of this goal, industrial-scale operational conditions introduce additional factors to batch solutions, including residence time, interaction of particulate flow with pipe walls, mixing, heat transfer dynamics, and microwave penetration depth of a moving flow (Morschhäuser et al., 2012; Qiao and Xie, 2016). Although there is growing interest in patented innovative designs for microwave continuous processing systems, such lab-scale systems remain uncommon due to their added complexity in multi-physics (Siddique et al., 2022). Although considerable research efforts have focused on comprehending the factors that influence microwave material processing (Serra et al., 2020; Reinosa et al., 2019), the widespread adoption of microwave continuous systems may be facing delays owing to the poorly understood dynamics of multi-physics. Low energy efficiency and inconsistent heating rates still mark the significant challenges of implementing a MWH system in industry. The widespread adoption of microwave continuous systems needs to address the poorly understood dynamics of multi-physics and call for precise control measures (Huayu et al., 2021).

Simulation tools have emerged as indispensable for exploring various conditions and outcomes, allowing for mathematical analysis of field patterns (Chen et al., 2022). For instance, a previous study (Ahmed, 2016) has delved into size and shape optimization of simulated materials to achieve specific temperature distributions. Efficient control of the microwave field has been demonstrated in Jung et al. (2021) to enable selective heating of samples while preventing undesired overheating. However, the complexity of modelling Maxwell's equations alongside convection–diffusion equations underscores the importance of studying uncertainty propagation and implementing advanced control solutions to manage resonant conditions (Curet et al., 2008; Vaz et al., 2014; Mimoso et al., 2017).

This study seeks to advance Microwave Continuous Processing Technology by enhancing the system performance. We investigate energy dynamics through numerical modelling of limestone calcination inside a simplified layout microwave continuous reactor. Specifically, we contribute by: (i) implementing effective control measures for energy usage; (ii) assessing the influence of tube orientation relative to the waveguide on *in-situ* energy dissipation (iii) elucidating the interactions between electromagnetic waves and thermal energy fields resulting from processing various material loads; (iv) evaluating the energy balance and efficiency of the system; and (v) discussing the impact of Microwave Continuous Processing Technology on Greenhouse Gas (GHG) emissions and its significance in the Cement Industry.

2. Governing equations

2.1. Electromagnetic model

Maxwell's equations are fundamental in electromagnetic theory, defining how electromagnetic fields are generated. When studying materials experiencing electric and/or magnetic polarization, the set in Eq. (1) accurately describes these phenomena, covering magnetic and electric fluxes and addressing dipole rotation and charge accumulation within the material (Griffiths, 2017).

$$\nabla \cdot \mathbf{D} = \rho_f \tag{1a}$$

$$\nabla \cdot \mathbf{B} = 0 \tag{1b}$$

$$\nabla \times \mathbf{E} = -\frac{\partial \mathbf{B}}{\partial t} \tag{1c}$$

$$\nabla \times \mathbf{H} = \mathbf{J}_f + \frac{\partial \mathbf{D}}{\partial t} \tag{1d}$$

where $\mathbf{D}$ is the electric flux density [C/m^2], ρ_f is the electric charge density [C/m^3], $\mathbf{H}$ is the magnetic flux density [Wb/m^2], $\mathbf{E}$ is the electric field [V/m], $\mathbf{B}$ is the magnetic field [A/m^2] and $\mathbf{J}_f$ is the electric current density [A/m^2].

The magnetic and electric fluxes correlate with the interacting fields through the additional constitutive set of Eq. (2).

$$\mathbf{D} = \varepsilon \mathbf{E} \tag{2a}$$

$$\mathbf{B} = \mu \mathbf{H} \tag{2b}$$

$$\mathbf{J}_f = \sigma \mathbf{E} \tag{2c}$$

where $\varepsilon = \varepsilon' - j\varepsilon''$ is the material's complex electric permittivity [F/m] and $\mu = \mu' - j\mu''$ is the material's complex magnetic permeability [H/m], and σ is the electric conductivity [S/m]. The complex properties quantify the material's affinity to polarize with the external electric field (ε) and magnetic field (μ). The real part is associated with the material's capacity to store potential energy, while the imaginary part reflects the momentum decay responsible for heat dissipation. Hence, for microwave heating of materials, a crucial requirement is a non-zero imaginary part of permittivity and/or permeability.

As a dielectric material, limestone will not conduct *free charges* ($\sigma = 0$) and interactions with the magnetic field are negligible ($\mu'' = 0$). The Helmholtz Eq. (3) is obtained by solving the Maxwell equations with the respective constitutive relations and assumptions made and considers properties relative to vacuum.

$$\nabla \times \frac{1}{\mu_r}(\nabla \times \mathbf{E}) - \tilde{k}^2 \varepsilon_r \mathbf{E} = 0 \tag{3}$$

where $\mu_0 = 4\pi \times 10^{-7}$ H/m and $\varepsilon_0 = 8.854 \times 10^{-12}$ F/m are the permeability and permittivity properties of vacuum, $\tilde{k}$ is the complex-valued wavenumber in vacuum, $\mu_r = \mu/\mu_0$ is the relative magnetic permeability, and $\varepsilon_r = \varepsilon/\varepsilon_0$ is the relative dielectric permittivity.

The electromagnetic heating source Eq. (4) is the volume (V) integral form of the Helmholtz Eq. (3).

$$Q_{EM} = \int_V \frac{\omega \epsilon_r''}{2} |\mathbf{E}|^2 dV \tag{4}$$

The penetration depth is an important measure that serves as an indicator of the distance from the material's surface at which the field strength decreases by 37%, precisely at $e^{-1} = 0.368$ (Sun et al., 2016). As the polarized molecules revert to their initial disordered state, electromagnetic energy is dissipated in the form of heat. The dielectric loss tangent in Eq. (5) characterizes the material's capacity to generate heat when interacting with electromagnetic energy.

$$\tan \delta_\epsilon = \frac{\epsilon''}{\epsilon'} \tag{5}$$

When a plane wave interacts with a lossy medium, the electric field changes and the waveguide wavelength changes according to Eq. (6) (Pozar, 2015).

$$\lambda_g = \frac{2\pi}{\Im(j\omega\sqrt{\mu\epsilon})} \tag{6}$$

2.2. Chemical model

Solid state reactions that are thermally stimulated can be kinetically described by Eq. (7) (Pérez-Maqueda et al., 2005).

$$\frac{d\alpha}{dt} = k(T) \cdot f(\alpha) \tag{7}$$

where α is the species' degree of conversion, t is time [s], and both $k(T)$ and $f(\alpha)$ describe the reaction rate dependency with temperature T [K].

The decomposition process in limestone calcination is described by the chemical reaction below and is activated within the temperature range of 823–1233 K (Csernyei and Straatman, 2016).

$CaCO_3(s) \longrightarrow CaO(s) + CO_2(g)$.

Limestone calcination was modelled by Eq. (8) as a continuous incompressible flow.

$$R_i = \rho \frac{\partial \omega_i}{\partial t} + \rho(\mathbf{v} \cdot \nabla \omega_i) \tag{8}$$

where R_i is each species i rate of reaction [kg/m^3 s], ρ is the density [kg/m^3], ω is the mass fraction and $\mathbf{v}$ is the velocity vector [m/s].

The kinetic rate for the decomposition of $CaCO_3$ was derived by Escardino et al. from experimental findings in Escardino et al. (2008) for particles with an average radius smaller than 120 μm. In their test setup, the decomposition of $CaCO_3$ took place in an air stream nearly free of CO_2, resulting in the rate expression in Eq. (9), which provided the best fit to the decomposition results.

$$\frac{d\alpha}{dt} = k(T) \frac{S_e}{c_B^0} c_B^{0\,1/3} (1-\alpha)^{1/3} \tag{9}$$

where S_e is the specific surface area of the calcite particle [m^3/m^2], and c_B^0 is the initial molar concentration of $CaCO_3$ [kmol/m^3]. The reaction rate dependency with temperature $k(T)$ is described by the Arrhenius Eq. (10).

$$k(T) = k_0\, e^{\left(-\frac{E_a}{RT}\right)} \tag{10}$$

where k_0 is the pre-exponential factor [kmol$^{2/3}$/(m min)], E_a is the activation energy [J/mol] and $R = 8.314$ J/(mol K) is the universal gas constant.

2.3. Thermal model

The thermal model serves as the linkage for all interfaces within the numerical model, as electromagnetic properties and chemical activation rely on temperature. Eq. (11) represents the transient energy state affected by convective and/or diffusive transport along with internal sources (Hanks, 2003).

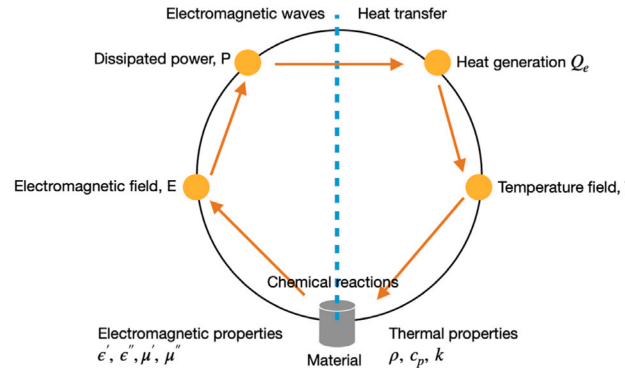

Fig. 1. Flux diagram of the interaction between the three participating interfaces.

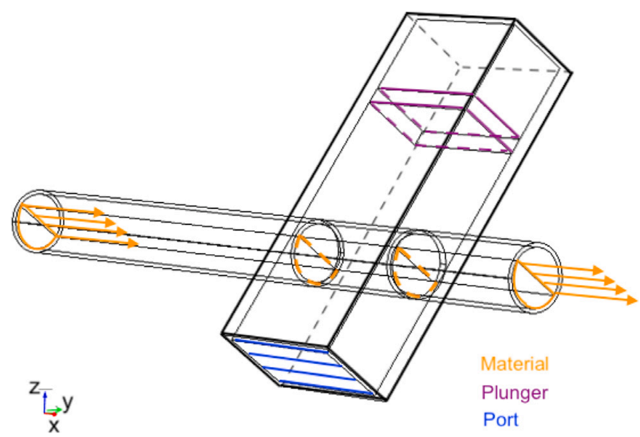

Fig. 2. 3D geometry model representation.

$$\frac{\partial}{\partial t}(\rho C_p T) + \mathbf{v} \cdot \nabla(\rho C_p T) + \nabla \cdot \mathbf{q} = Q \tag{11}$$

where C_p is the specific heat at constant pressure [J/(kg K)], q is the heat flux [W/m^2] and Q is the heat source [W/m^3]. The local heat flux density ($\mathbf{q}$) is governed by Fourier's law of thermal conduction: $\mathbf{q} = -\kappa \nabla T$, where κ is the thermal conductivity [W/(m K)].

The integral form of the energy balance, as described by Eq. (12a), governs the cumulative quantity of each transport term within a control volume (Bobok, 1993).

$$EB_1 + EB_2 - EB_3 - EB_4 = 0 \tag{12a}$$

$$EB_1 = \int_V \mathbf{v} \cdot \nabla(\rho C_p T)\, dV \tag{12b}$$

$$EB_2 = \int_S h(T - T_0)\, dA + \int_S (-\kappa \nabla T) \cdot \hat{\mathbf{n}}\, dA \tag{12c}$$

$$EB_3 = Q_{EM} \tag{12d}$$

$$EB_4 = \int_V |\mathbf{v} \cdot \nabla \alpha|\, (-\Delta H)\, \rho\, dV \tag{12e}$$

where h is the convection coefficient [W/(m^2 K)], $T_0 = 293.15$ K is the ambient temperature, $\hat{\mathbf{n}}$ is the vector normal to the surface, Q_{EM} is the electromagnetic heating source [W], and ΔH is the enthalpy of reaction [J/kg].

Table 1
Design parameters considered for the 3D model.

Parameter	Value
Tube diameter D_i [mm]	34
Tube thickness [mm] (Mastorakos et al., 1999)	5
Tube length [mm]	$5 \times a$
Cavity cross sectional width a [mm]	86.36
Cavity cross sectional height b [mm]	43.18
Cavity length [mm]	225
Cavity thickness [mm]	10
Plunger thickness [mm]	10
Insulation thickness [mm]	25
Dynamic angle of repose ϕ_D [°] (Henein et al., 1983)	34.9

Table 2
Limestone kinetic properties (Escardino et al., 2008).

Parameter	Value
Apparent density ρ [kg/m^3]	2270
Specific area S_e [m^2/m^3]	1.365×10^6
Frequency factor k_0 [kmol$^{2/3}$/(m min)]	367
Apparent activation energy E_a [J/mol]	175 384

3. Coupled multiphysics model

The finite element software COMSOL Multiphysics® (version 5.1) was employed to simulate the electro-magneto-thermal phenomenon in real-time mode. COMSOL facilitates the analysis of electromagnetic waves in the frequency domain, heat transfer within solids, and the transport of concentrated species.

The coupling of the physical phenomena involved in limestone decomposition and microwave heating is illustrated in Fig. 1 (Kopyt and Celuch, 2006). This linked process was explored using the 3D representation of the MW system depicted in Fig. 2. In this setup, a single-mode TE01 wave moves through the rectangular cavity, filled with air at atmospheric pressure. This cavity acts as the standard WR-340 waveguide and operates at a frequency of 2.45 [GHz]. Limestone, initially at room temperature, enters and gets heated as it moves through the tube that crosses the rectangular cavity. The tube might be partially or entirely filled with material, demonstrated in Fig. 2 with a 50%-fill ratio. Insulation was applied to the outer boundaries of the structure, made from a glass fibre material with dielectric and thermal properties sourced from (Modarresifar et al., 2016; Rossi and Rocco, 2014).

The three-dimensional design accounts for the rotary bed motion typically observed in conventional kiln operations. The dynamic angle of repose ϕ_D (measured concerning the gravity vector in the z-axis) was derived for the bed of material based on experimental measurements by Heinen et al. (Henein et al., 1983). According to the authors, the dynamic angle of repose ϕ_D remains unaffected by bed depth or rotational speed. In this study, it is appropriate to approximate the rolling bulk bed as a collection of particles with irregular shape and an average radius of approximately 100 [μm], along with the cylinder diameter considered. All design dimensions are outlined in Table 1. Limestone kinetic properties are presented in Table 2, dielectric properties were obtained from (Behrend et al., 2016) and thermal properties from (Komarov, 2012).

The dielectric constant plays a crucial role in the electromagnetic energy balance of the system (Catalá-Civera et al., 2015). As limestone's ability to absorb electric energy changes with temperature, it affects the impedance of the loaded cavity, highlighting the importance of impedance matching control. Inspired by Mimoso's groundbreaking study on the continuous microwave processing of glass melting (Mimoso et al., 2017), the model integrates a plunger that reflects the electric field within the rectangular cavity. This plunger can assume various positions to continuously fine-tune the cavity's impedance and requires sweeping over only half the value of λ_g due to the periodic nature of the electromagnetic wave. Although impedance matching is crucial in microwave experiments, it is not directly available in current computational tools and necessitates an external numerical procedure. The controller was integrated into the COMSOL model through LiveLink™ for MATLAB®, enabling continuous adjustments of the plunger position and the imposition of input energy (Eq. (13)) for the coupled system. The latter is vital for maintaining numerical stability, achievable by fixing one or more terms in Eq. (13) to converge to a single condition. A singular solution for the bed outlet temperature correlates with a fixed and converged decomposition α. Consequently, Eq. (13) considers the theoretical consumption for the reaction $Q_{\alpha,t} = 0.999\, \dot{m}\, \Delta H$ to enforce 99.9% limestone decomposition.

$$P_{\mathrm{MW}} = \frac{\dot{m}\, C_p\, \Delta T + 0.999\, \dot{m}\, \Delta H + P_L}{\eta_{\mathrm{MW}}} \tag{13}$$

where P_{MW} is the energy for wave excitation [W], $\dot{m}$ is the mass flow rate [kg/s], P_L is the energy lost though heat transfer [W], and $\eta_{\mathrm{MW}} = \mathrm{EB}_3/\mathrm{P}_{\mathrm{MW}}$ is the electromagnetic efficiency.

The modelling included the simulation of chemical species transport within the bed of material, depicted in orange in Fig. 2. Heat transfer was taken into account across all domains, while the physics of electromagnetic waves were specified in all domains except for the insulation domain and the area behind the plunger. Initial conditions (with subscript ini) are summarized below. Boundary conditions were defined for the electromagnetic interface (items 1. and 2.), for the transport of concentrated species (items 4., 5. and 6.) and for the thermal interface (items 7., 8. and 9.).

- Initial decomposition of $CaCO_3$ is zero: $\alpha_{ini} = 0$.
- Initial electric field is zero: $\mathbf{E}_{ini} = 0$.
- Within the bed, T_{ini} increases linearly from 300 K at the inlet to 1200 K at the outlet, while for the remaining domains is maintained at 300 K.

1. A transverse electric single-mode wave (TE10) is excited with P_{MW} at the blue boundary in Fig. 2;
2. A perfect electric conductor condition on every boundary: $\hat{\mathbf{n}} \times \mathbf{E} = 0$.
3. Prescribed $CaCO_3$ decomposition at the inlet: $\alpha = 0$;
4. Prescribed null diffusive flux at tube's outlet: $-\hat{\mathbf{n}} \cdot D_i \nabla \omega = 0$;
5. Prescribed zero flux at the remaining material boundaries: $-\hat{\mathbf{n}} \cdot (\rho v \alpha)$.
6. Tube's inlet temperature: $T = 300$ K;
7. Null energy flux at tube's outlet: $-\hat{\mathbf{n}} \cdot \mathbf{q} = 0$;
8. Convective heat exchange with the exterior: $-\hat{\mathbf{n}} \cdot \mathbf{q} = h(T_{ext} - T)$, where $T_{ext} = 273.15$ K is the exterior temperature. Free convection correlations were used and considered geometry inclination (Bergman et al., 2011; Yilmaz et al., 2005) .

3.1. Validation and verification issues

A prerequisite to trust the numerical solution is Validation and Verification. Validation aims to compare the numerical solution with real-world data obtained from equipment or well-established theories. On the other hand, verification focuses on ensuring the accuracy of the solutions to the equations themselves.

The thermal-Maxwell model, as implemented in COMSOL, has been rigorously verified and validated in prior studies, particularly concerning static materials. Notably, the work of Vaz et al. (2014) provides significant validation in this regard. Consequently, numerical validation cases do not go beyond those available for limestone.

3.1.1. Chemical kinetic model

The decomposition rate of limestone is modelled with Eq. (9), utilizing properties detailed in Table 2, covering five different temperatures.

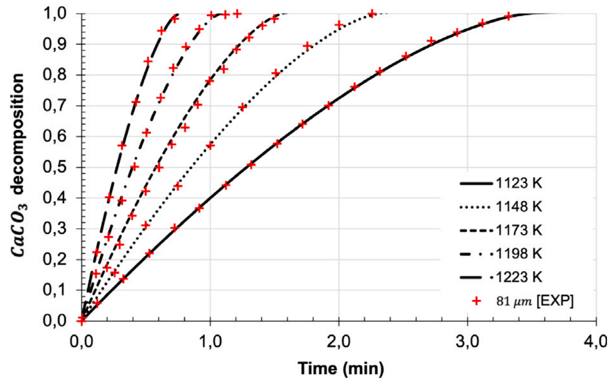

Fig. 3. Validation of numerical results with experimental data (Escardino et al., 2008).

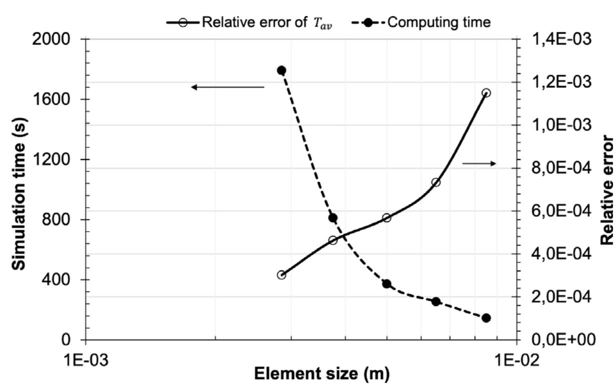

Fig. 4. Relative error decay for the average temperature T_{av} of the bed of material and computing time t [s] as a function of the mesh element size.

The corresponding evolution of limestone decomposition is illustrated in Fig. 3, juxtaposed with experimental data from (Escardino et al., 2008). The reliability of the rate expression from Eq. (9) is corroborated by numerical results that closely align with the experimental points.

Comsol employs a time-dependent solver, with the time-step adapting according to the relative tolerance. Hence, investigating the influence of the time-step on the chemical kinetic model equation was not necessary for the validation of the chemical kinetic model.

3.1.2. Mesh refinement study

A mesh refinement analysis was conducted using the 3D model, accounting for an 80% fill ratio of material within the tube. Five numerical solutions were derived using various mesh configurations characterized by base sizes $h_{i=1,2,3,4,5}$. The diminishing relative error in temperature and solver time concerning mesh element size is depicted in Fig. 4.

The maximum relative error (1.15×10^{-03}) corresponds to the coarser mesh with a higher base size ($h_5 = 8.50\times10^{-03}$ [m]), whereas the minimum relative error (3.02×10^{-04}) corresponds to the finest mesh with a lower base size ($h_1 = 2.85\times10^{-03}$ [m]). Despite the refinement ratio maintaining an approximate consistency across different meshes, the distribution is not uniform throughout the entire domain. This discrepancy explains the non-linear error decay and the considerable increase in computation time of almost 20 times between the coarser and finer meshes considered. However, it is feasible to discern a monotonic convergence index that validates the reduction of the discretization error based on Richardson extrapolation (Roy, 2005). Relative errors remain below 1.20×10^{-03}, which is deemed acceptable for engineering purposes.

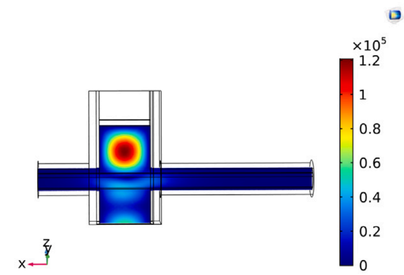

(a) Electric field norm distribution.

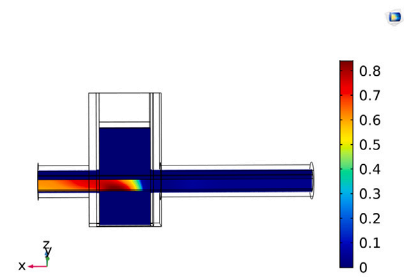

(b) Loss factor distribution.

Fig. 5. Simulation results of electric field varying sinusoidally along the direction of material propagation.

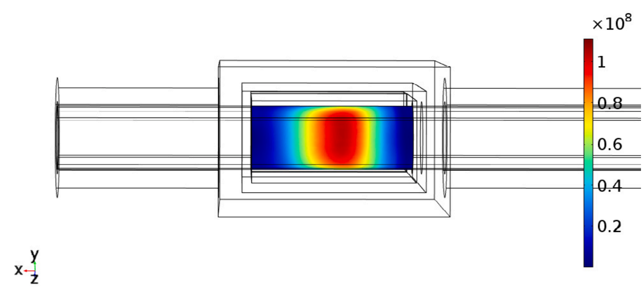

(a) Electromagnetic wave propagating perpendicular to bed inclination.

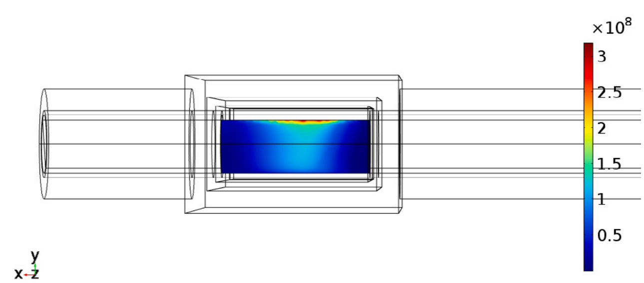

(b) Electromagnetic wave propagating in z-axis.

Fig. 6. Electromagnetic energy density distribution [W/m^3].

4. Discussion of the results

The results are focused on material interactions with the electric field, assessing the performance and energy efficiency of microwave continuous processing applied to limestone. The approach involves comparing five tube fill-ratios of material: 30%-fill, 50%-fill, 65%-fill, 80%-fill, and 100%-fill. The settling velocity was determined based on the maximum temperature required for the calcination reaction, which is 1233 K (Csernyei and Straatman, 2016). Through numerical

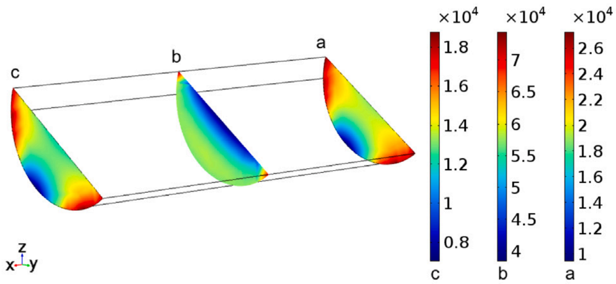

(a) 30%-fill ratio.

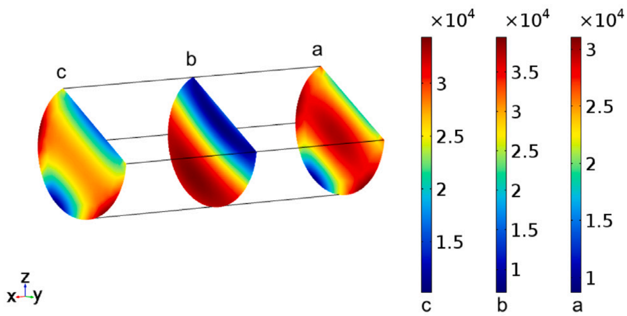

(b) 80%-fill ratio.

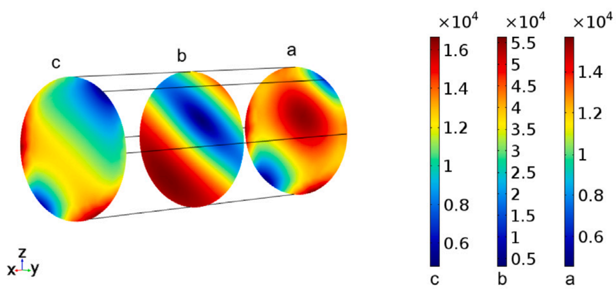

(c) 100%-fill ratio.

Fig. 7. Electric field distribution [V/m].

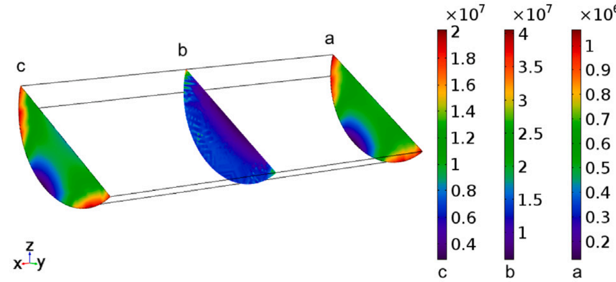

(a) 30%-fill ratio.

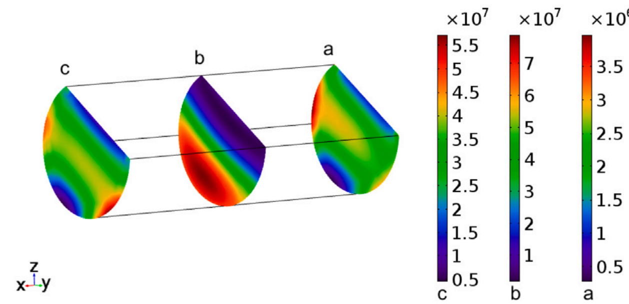

(b) 80%-fill ratio.

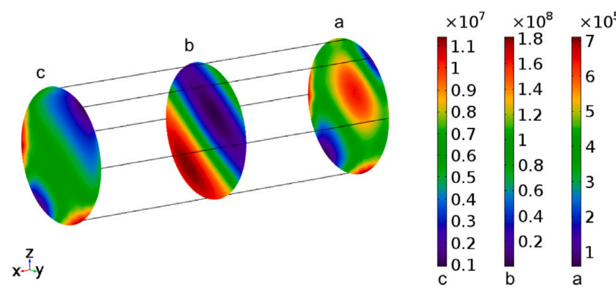

(c) 100%-fill ratio.

Fig. 8. Electromagnetic heating source distribution [W/m^3].

experimentation based on the fully filled tube, it was established that an imposed material velocity of $\upsilon = 5.3\times10^{-4}$ m/s accurately reproduces this temperature as per the reference of the chemical model.

4.1. Electric field and material interactions

As a dielectric material, limestone undergoes polarization when subjected to an external electric field $\vec{\mathrm{E}} = \hat{\mathrm{n}}\,\mathrm{E}$, accumulating potential energy as it attempts to align with the direction $\hat{n}$ of the applied field (Vilchevskaya and Müller, 2021). The stored energy, as described by Eq. (4), dissipates in the form of a heating source in the energy Eq. (11). It involves the combined intensity of the electric field norm and temperature values, adjusted by limestone's dielectric loss properties responsible for the material's temperature elevation.

The impact of tube orientation concerning the rectangular cavity on the specific location of energy dissipation is discussed. Only two configurations are viable within the model geometry depicted in Fig. 2. A first scenario, modelled by Mendes (2017), is the tube aligned with the smaller side of the cavity (of size b) where the distribution of dielectric loss response, relevant for decomposition, occurs outside the cavity domain. The second scenario, adopted in this work and illustrated in Fig. 5, exhibits the tube aligned with the widest side of the cavity (with size a). Here, the pertinent distribution of the loss factor for limestone decomposition is observed within the cavity domain in Fig. 5(b). Mathematically, the sinusoidal projection of the TE10 electric field onto the bed of material, illustrated in Fig. 5(a), is responsible for maintaining the maximum value of dielectric loss around the middle plane of the cavity. The configuration in Fig. 5 offers a direct advantage by facilitating *in situ* energy dissipation in that region, thereby avoiding the necessity for excessive tube length to meet material decomposition requirements and reducing associated energy costs related to thermal losses.

The impact of electromagnetic wave projection onto the bed of material becomes evident in Fig. 6, showcasing the electromagnetic energy density. This influence is demonstrated in two cases: the TE10 wave propagating perpendicular to the bed's inclination, as seen in Fig. 6(a), and vertically in the z direction, depicted in Fig. 6(b). The distribution of electromagnetic energy density noticeably varies based on the area of the bed's surface normal to the direction of wave propagation. Notably, in Fig. 6(b), where high energy concentration is observed, the energy density is three times higher than in the other scenario. The issue of concentrated and intense energy dissipation holds significance as it subjects the material to steep energy gradients, potentially leading to temperature-related challenges known as thermal runaways (Ramos et al., 2021). This concern is particularly critical in microwave heating processes involving materials like limestone, that are characterized by low thermal conductivity and a dielectric loss

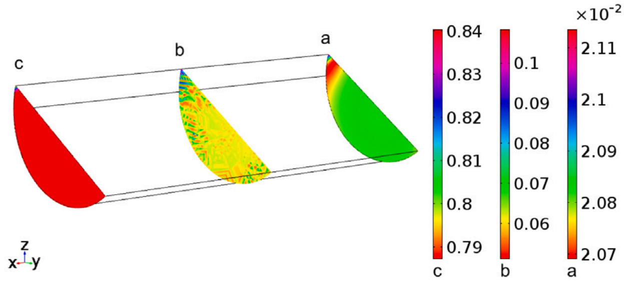

(a) 30%-fill ratio.

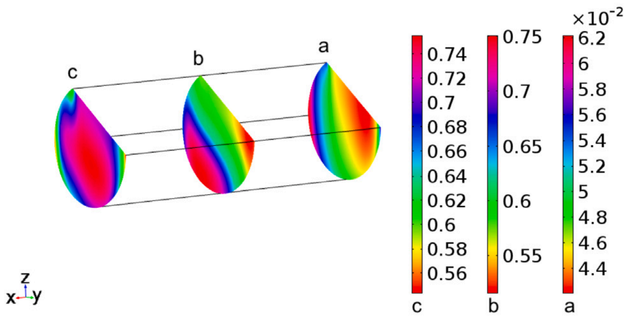

(b) 80%-fill ratio.

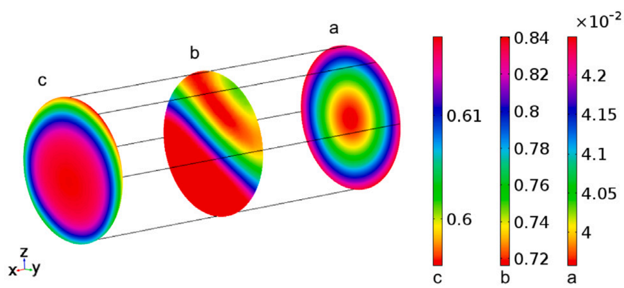

(c) 100%-fill ratio.

Fig. 9. Loss factor distribution.

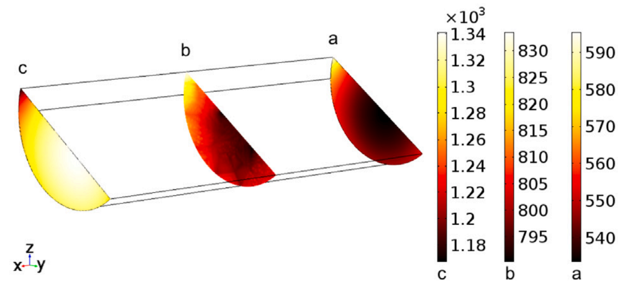

(a) 30%-fill ratio.

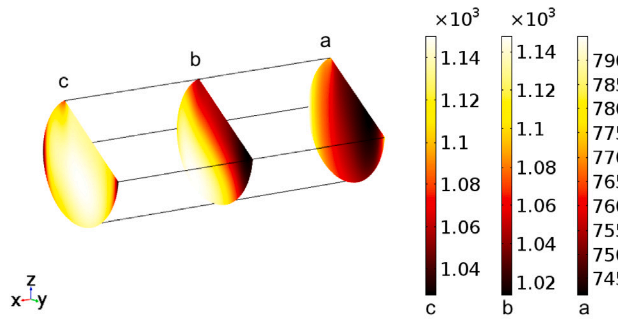

(b) 80%-fill ratio.

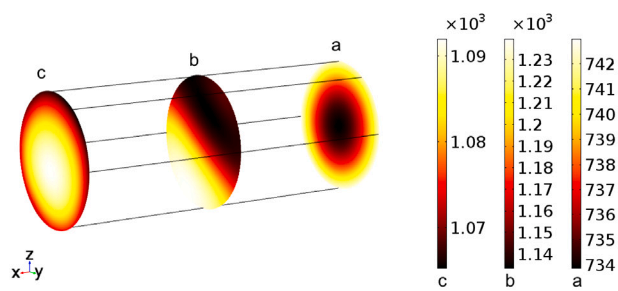

(c) 100%-fill ratio.

Fig. 10. Temperature distribution $T\,[K]$.

response that amplifies with temperature. Such materials are more susceptible to challenges arising from intense and concentrated heating sources. Hence, meticulous attention is necessary when managing these systems.

The upcoming results examine simulations where the electromagnetic wave propagates perpendicular to the bed of material's inclination. This approach is adopted to mitigate potential numerical instabilities arising from the thermal model. Additionally, the study evaluates the variation of the electric field along the direction of material propagation, a factor found to significantly influence *in situ* energy dissipation.

4.2. Fields distribution analysis

Analysis of the participating fields is conducted for five simulated tube fill-ratios of material. Fig. 7 displays the electric field, Fig. 8 illustrates the electromagnetic heating source, Fig. 10 showcases the temperature distribution, and Fig. 9 represents the loss factor. Each figure exhibits the results corresponding to the 30%-fill, 80%-fill, and 100%-fill ratios, illustrated in three perpendicular slices aligned with the axial velocity and positioned at the beginning, middle, and end of the bed of material within the rectangular waveguide (see Fig. 2).

Table 3
Temperature field related results.

$\%-fill$	30	50	65	80	100
$T_{av}\,[K]$	936	1082	1041	1029	1007
$T_{max}\,[K]$	1405	1201	1203	1188	1239
$\sigma_{T_{av}}\,[K]$	310	113	153	133	185

Furthermore, Table 3 compiles the numerical results for each load, encompassing: (i) average temperature $T_{av}\,[K]$, (ii) maximum temperature $T_{max}\,[K]$ and (iii) the standard deviation of temperature within the bed $\sigma_{T_{av}}\,[K]$.

The distributions of the electric field norm $|\mathbf{E}|$ and the electromagnetic heating source Q_{EM} are depicted in Figs. 7 and 8. Due to the imposition of the TE10 mode at the port boundary and the model configuration, higher intensities of the electric field are sustained at the central slice b. According to Eq. (4), this confirms the desired dissipation of electromagnetic energy occurring *in situ*. The penetration of microwaves is evident at this slice, encompassing approximately 30% of the bed for 50%-fill, 65%-fill, and 80%-fill, and around 45% for 100%-fill before experiencing the 37% reduction in field strength.

The dielectric loss factor acts as the conduit for electromagnetic energy entering the thermal energy balance, thereby governing the electric and thermal response of the system. The increasing loss factor

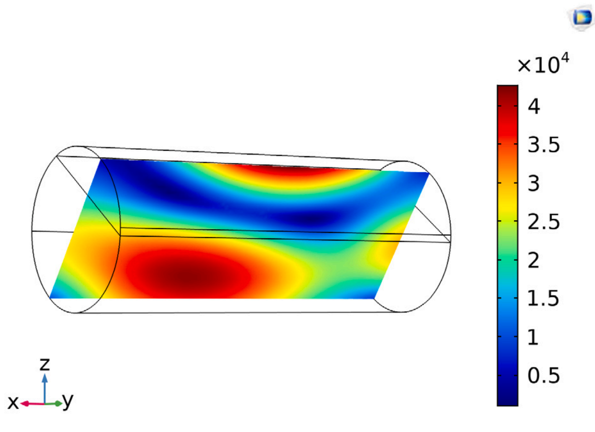

(a) Electric field distribution.

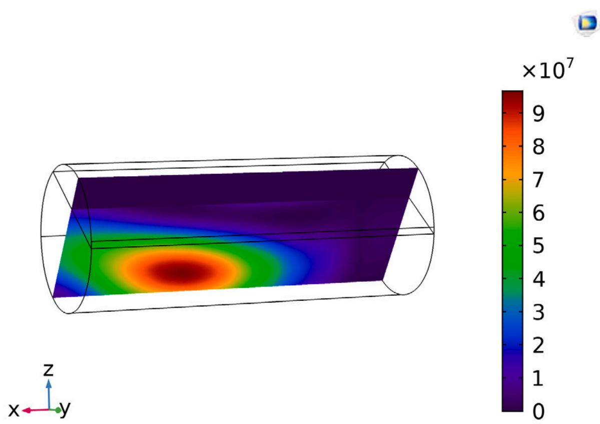

(b) Electromagnetic heating source distribution.

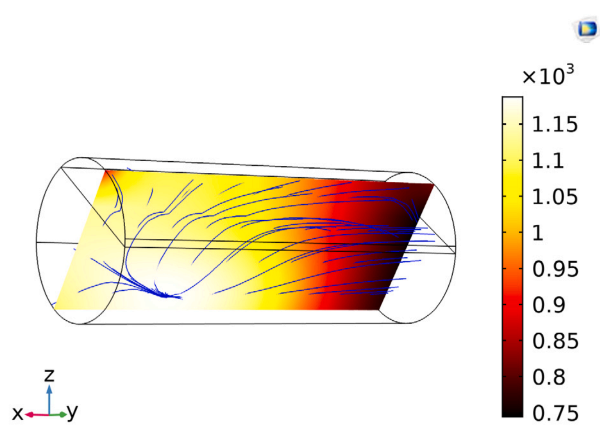

(c) Temperature field distribution and temperature gradient lines.

Fig. 11. 80%-fill ratio.

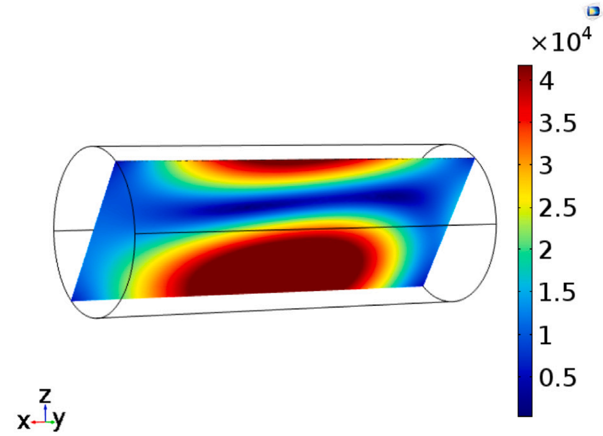

(a) Electric field distribution.

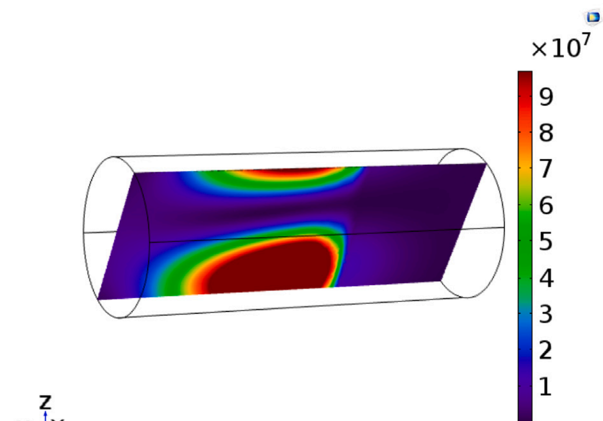

(b) Electromagnetic heating source distribution.

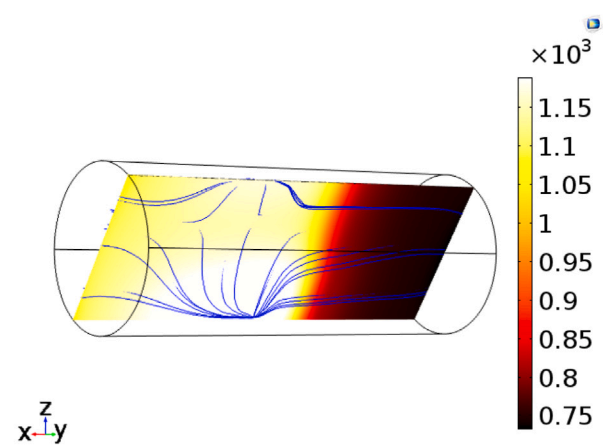

(c) Temperature field distribution and temperature gradient lines.

Fig. 12. 100%-fill ratio.

of limestone with temperature leads to distributions in Figs. 9 and 10 being quite similar. Limestone starts to dissipate significant amounts of absorbed electromagnetic energy as heat only above 800 K (Behrend et al., 2016). Below this temperature, limestone exhibits low losses, as observed in slice a, and the strong imposition of the electromagnetic field does not result in significant electromagnetic dissipation as in the case of slice b. For tube fill-ratios of 80%-fill and 100%-fill, the maximum loss factor reaches $\varepsilon'' \approx 0.8$. In the temperature range of $1000-1200\,[\mathrm{K}]$, the dielectric constant of limestone is approximately $\varepsilon' \approx 3.4$. Consequently, this yields a dielectric loss tangent value (Eq. (5)) of $\tan_{\delta_\varepsilon} \approx 0.24$, indicating the material's potential for adequate heating at microwave frequencies (Shah, 2018).

According to Table 3, the attained maximum temperatures fall within the limestone decomposition temperature range $(823-1233, [\mathrm{K}]$

(Csernyei and Straatman, 2016)), validating the selection of the axial velocity. These temperatures are reached at slice b, positioned in the middle of the cavity. Notably, for the 30% fill-ratio the maximum temperature is accomplished at $x_{T_{max}}$ = 90% and exceeds the 1233 K, which is a result from Eq. (11) being governed by the convective transport. Adjusting the velocity to lower the maximum temperature could promote radial temperature growth, although at the expense of reduced thermal efficiency. For the remaining loads, as the penetration of microwaves is limited to 30%–45% of the bed's height, with the field strength decreasing until it nearly vanishes, the remaining portion is not equally heated by the dissipation of electromagnetic energy. Instead, heat is primarily convected through bed rotation, as is customary in conventional kilns to promote radial temperature uniformity. This is particularly necessary because limestone conductivity decreases with temperature and remains relatively low. The effectiveness of bed rotation is demonstrated in Table 3 by temperature standard deviations measuring below 18% of T_{av}, affirming the desired uniformity achieved by the selected model configuration. The temperature distribution in Fig. 10 remains relatively constant across each cross-section while displaying variation along the longitudinal axis.

To comprehend longitudinal variations, this qualitative analysis is supplemented with distributions of the electric field, electromagnetic heating source, and temperature for the scenarios of 80%-fill as shown in Fig. 11 (which includes the air domain inside the tube in Fig. 11) and 100%-fill in Fig. 12. The periodic propagation of the electromagnetic wave within the material bed is evident in the case of 100%-fill, whereas for 80%-fill the electric field deviates from the anticipated TE10 mode. Differences in temperature distribution between 80%-fill and 100%-fill shed light on the electric field's distribution, owing to the distinct heat transfer mechanisms for the bed and tube in both cases. While the mechanism remains axisymmetric for the 100%-fill scenario, lower fill-ratios lose this symmetry.

Furthermore, the maximum dissipation of electromagnetic energy and the peak magnitude of the electric field occur simultaneously as the temperature approaches its maximum value. This synchronization is attributed to the dielectric loss of limestone, that increases with temperature and typically reaches its peak around 1200 K. According to Eq. (4), this scenario should optimize the utilization of the available energy supplied to the microwave continuous unit. The maximum dissipation of electromagnetic energy occurs when Eq. (14) is satisfied and could never precede the peak magnitude of the electric field because impedance matching control is employed and the energy input to the system - Eq. (13) - is predetermined, considering that limestone calcination is an endothermic reaction, coupled with the fact that the dielectric loss increases with temperature ($d\varepsilon/dT > 0$). Hence, impedance matching control and predefining the P_{MW} for limestone proves to be a crucial strategy in preventing energy dissipation before reaching the maximum magnitude of the electric field. With this ensured, Eq. (14) clearly suggests that the maximum values for dissipation of electromagnetic energy, electric field intensity and temperature will always coincide due to $d\varepsilon/dT > 0$.

$$\frac{dQ_{EM}}{dx} = 0 \rightarrow \frac{1}{E}\frac{dE}{dx} = -\frac{1}{2\varepsilon}\frac{d\varepsilon}{dT}\frac{dT}{dx} \tag{14}$$

The dynamic interplay between diffusive and convective transport mechanisms, influenced by bed rotation and axial development, dictates whether electromagnetic dissipation occurs concurrently with the peak magnitude of the electric field or upstream, as in the 30%-fill case. The term $\rho C_p u_x$ governs the axial development of energy. Variations in the terms affecting the transport mechanisms, apart from influencing the predefined energy requirement of the system, will primarily affect the proximity of electromagnetic dissipation to the peak magnitude of the electric field. The temperature gradient streamlines in Figs. 11 and 12 illustrate how the tubes' fill-ratio predominantly influences the diffusive term, given limestone's predetermined thermal conductivity and the rotational dynamics of the bed. As the velocity was set based on a fully filled tube, lower fill ratios entail an excess of energy beyond the minimum processing requirement, which the diffusive term absorbs.

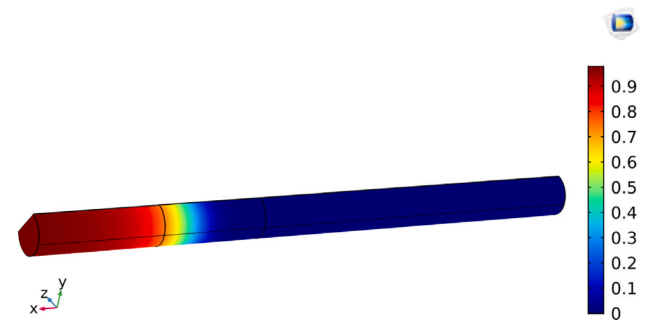

Fig. 13. Axial evolution of limestone decomposition for 80%-fill ratio.

Table 4
Integral energy balance.

	30% fill	50% fill	65% fill	80% fill	100% fill
EB_1 [W]	179.15	319.74	507.61	562.30	674.47
EB_2 [W]	134.14	147.10	158.99	189.31	202.62
EB_3 [W]	904.01	1451.37	1946.48	2326.85	2846.15
EB_4 [W]	−602.13	−981.94	−1277.88	−1547.78	−1967.05
Res_{abs} [W]	11.41	−2.59	−2.01	−27.47	−2.01
Res_{rel}	0.013	0.002	0.001	0.012	0.001

Table 5
Heat absorbed during the chemical reaction.

	30% fill	50% fill	65% fill	80% fill	100% fill
$\lvert\dot{Q}_\alpha\rvert = \lvert EB_4\rvert$ [W]	602.13	981.94	1277.88	1547.78	1967.05
$\dot{Q}_{\alpha,t} = 0.999\,\dot{m}\,\Delta H$ [W]	590.72	984.53	1279.90	1575.20	1969.10
Relative error	0.019	0.003	0.002	0.017	0.001

Thus, the unique phenomenon observed in the 80%-fill scenario illustrated in Fig. 11 stems from the interplay between heat transfer and the electromagnetic field across diverse mediums – the dielectric material and air – combined with the surplus energy absorbed by the diffusive term.

4.3. Integral energy balance

The integral energy balance from the set of Eq. (12a) serves as an indicator of the system's performance. In Table 4, the resultant energy balance for each tube fill-ratio is listed. The absolute residue, computed as $Res_{abs} = EB_1 + EB_2 - EB_3 - EB_4$, should ideally be zero as per Eq. (12a). The relative residue, defined by $Res_{rel} = |Res_{abs}|/\max(|EB_1|, |EB_2|, |EB_3|, |EB_4|)$, attained values lower than 1.3%, indicating that the 3D calculations were corrected and align with the nearly zero residual. As anticipated, the heat term increases proportionally with the tube's fill-ratio.

The axial decomposition of limestone is displayed in Fig. 13 for the 80%-fill ratio. Additionally, Table 5 outlines the numerical errors associated with the energy consumption $\dot{Q}_\alpha$ relative to the theoretical value $\dot{Q}_{\alpha,t}$ set by the control algorithm for the defined 99.9% of material decomposition. Relative errors below 2% indicate the accurate implementation of the control algorithm. The energy consumed by the calcination reaction accounts for approximately 70% of the total energy, evidencing the substantial impact of the endothermic reaction on convergence history and numerical outcomes in continuous processing with MWH. At this juncture, impedance and energy input control emerged as pivotal integrated components ensuring the desired material decomposition while upholding heating efficiency. This aspect is critical for the numerical stability of the coupled convection–diffusion transport equations and Maxwell equations.

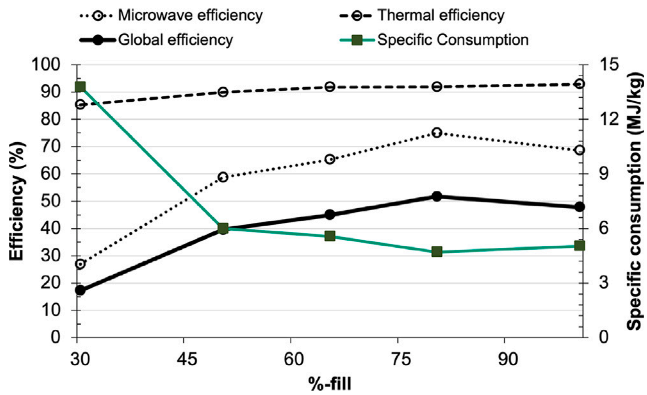

Fig. 14. Efficiencies and specific consumption for the simulated fill-ratios.

4.4. Efficiency analysis

Efficiency analysis is crucial for pinpointing essential operational aspects for enhancing microwave technology and determining its viable applications in the continuous processing of very-high temperature materials.

The efficiencies under the specified conditions are depicted in Fig. 14. Thermal losses of the system are quantified by the thermal efficiency η_T in Eq. (15), while electromagnetic losses are calculated through the microwave efficiency η_{MW} in Eq. (16). These metrics, in conjunction with the magnetron efficiency η_M (Vyas et al., 2015), collectively define the system's global efficiency η_G as described in Eq. (17). Additionally, the specific consumption C_e [MJ/kg] in Eq. (18) represents the total energy required for material decomposition.

$$\eta_T = 1 - \frac{EB_2}{EB_3} \tag{15}$$

$$\eta_{\mathrm{MW}} = \frac{EB_3}{P_{\mathrm{MW}}} \tag{16}$$

$$\eta_G = \eta_T \cdot \eta_{\mathrm{MW}} \cdot \eta_M \tag{17}$$

$$C_e = \frac{P_{\mathrm{MW}}/\eta_M}{\dot{m}} \tag{18}$$

The automatic control of operational parameters considered both thermal and microwave efficiencies. The encouraging thermal efficiency values (≈90%) likely stem from the volumetric heating and continuous convective processing (Das and Banik, 2021). The consistent trends observed in electromagnetic and global efficiencies result from the relatively constant thermal efficiency values. The global efficiency increases with the material load, reaching its maximum with the 80%-fill scenario. In contrast, specific consumption, which inversely relates to the global efficiency, reaches its lowest value $C_e = 4.7\,\mathrm{MJ/kg}$ for the same load. These outcomes suggest that microwave continuous processes can benefit from larger material loads, in line with earlier research (Bermúdeza et al., 2015), and hint about the existence of an optimal material fill-ratio.

4.5. Microwave continuous processing unit in the cement industry

The cement sector carries the highest total CO_2 emissions among all energy-intensive industries. A notable portion of these emissions is intrinsically linked to the calcination of limestone, which accounts for 50% of the total CO_2 emissions from cement production. Fossil fuel combustion in conventional kilns is responsible for 40%, while the remaining 10% is attributed to indirect factors (Naqi and Jang, 2019). Microwave technology serves as an alternative fuel technology exclusively aimed at reducing the 40% of total CO_2 emissions from cement plants attributed to fossil fuels: coal, oil, and gas. Implementing microwave technology in energy-intensive industries would require high operational efficiency and continuous access to real-time renewable energy sources such as hydropower, solar, wind, biomass and waste, geothermal, wave, and tidal energy.

The significant influence of the top five cement-producing countries in Europe is evident in their collective GHG emissions (European Commission and Directorate-General for Internal Market, Industry, Entrepreneurship and SMEs, 2018). Notably, one country alone contributed around 3.3 million tons of CO_2 emissions from fossil fuel combustion during clinker production in 2019 (Wojtacha-Rychter et al., 2021). Specific energy consumption C_e Eq. (18) serves as a valuable measure for deposited energy, aiding in the comparison between CH and MWH methods. In the context of limestone decomposition, the energy consumption of our simulated microwave continuous heating system is notably contingent on the rate of processed load. Minimizing energy consumption is critical in curtailing GHG emissions, and our numerical findings advocate for the advantage of microwave continuous processing with higher material loads in achieving this objective. Henceforth, for comparison purposes, the baseline value of emissions $0.33\,\mathrm{kg}$ of $CO_{2_{eq}}$ per kg of $CaCO_3$ is assumed for CH, whereas MWH emissions are derived from multiplying the specific consumption numerical results obtained for the 80%-fill scenario with the emission factor for electricity production in each country (Agency, 2023a). Note that the efficiency of mains electricity to microwave generation is accounted for through the magnetron efficiency η_M in Eq. (18).

Despite the majority of EU countries with competitive cement and lime sectors reported 44% of electricity production from renewable and nuclear sources in 2020, the adoption of the Microwave Continuous Processing Technology with ≈50% of global efficiency in processing limestone does not significantly aid in reducing $\mathrm{kg}_{CO_{2_{eq}}}/\mathrm{kg}_{CaCO_3}$ for these nations (Ritchie and Roser, 2020). Urgent steps need to be taken to curtail clinker production, particularly to counterbalance the heavy reliance on crude oil and natural gas for electricity generation. Countries like Sweden, France, Spain, or Portugal, that have been demonstrating the most substantial increase in renewable energy consumption, are promising candidates for the industrial implementation of a Microwave Continuous Processing Technology (Agency, 2023c). In particular, the efficient microwave continuous system would prosper in countries like France and Sweden, with 80% and 97% reduction of GHG emissions from fossil fuel combustion in clinker production.

While promising, the adoption of MWH to replace CH faces significant barriers in industry. Broadly, these can fit into two areas: process control and scalability. The MWH process control and scalability barrier will primarily hinge on the product processing requirements, advancing as quickly as experimental and numerical modelling expertise align (Goyal et al., 2022). The interdisciplinary complexity of MWH processing complicates reproducibility and underscores the need for a profound understanding of (i) electric fields in matter, electromagnetic waves and cavity resonators, (ii) heat transfer and fluid dynamics – considering that gases are likely always involved – and (iii) chemistry and physics of materials (Griffiths, 2017). Limestone calcination is an endothermic process, requiring a continuous supply of heat, while under- or over-burning of limestone must be avoided. Real-time temperature measurements inside a microwave oven for process monitoring are challenging. Fibre optics can measure inside a microwave cavity but are expensive and very fragile. Additionally, the success of IR thermometer readings depends on prior knowledge of material emissivity.

In relation to multimode applicators, a single-mode cavity resonator can offer significantly higher electric field strengths to achieve greater energy dissipation in the workload. While these applicators are constrained in size by the chosen wavelength and waveguide, processing large volumes of material is feasible through innovative conceptual designs that combine multiple applicators (Patil et al., 2014; Huayu et al., 2021). However, besides temperature and chemical composition, factors such as moisture content, grain size, and bulk density significantly influence the dielectric properties, thereby impacting material heating performance under MW energy (García-Baños et al., 2016). To achieve successful automation control of the process, either the input product must be defined beforehand, providing information to the system, or the system must be equipped to adjust to variations in these properties within a processing band range based on final product requirements. Furthermore, addressing fluctuations in supply voltage and ensuring frequency stability and energy requirements should not pose a barrier, as MW technology and voltage stabilizers are well-developed.

The rationale behind investing in a microwave processing unit to achieve energy savings stems from the inefficiency of conventional kilns. However, it may not be cost-effective to replace conventional kilns with a microwave processing unit for limestone processing. The production cost of one tonne of limestone is approximately \$109, with 50% attributed to fuel consumption (Ochoa George et al., 2010). This translates to a relatively low cost of 0.05€/tonne of limestone produced in conventional kilns. According to the specific consumption obtained for the 80%-fill case, it implies that the electricity cost would need to be lower than 0.038€/kWh for energy-cost savings to outweigh fuel consumption costs in limestone conventional production.

As industries strive for enhanced performance, cost competitiveness, and eco-friendly practices in line with circular economy principles, the Microwave Continuous Processing Unit's emergence in the cement industry is a development worth monitoring. Many strategies to mitigate CO_2 emissions from core processes, such as limestone calcination and fossil fuel combustion, could probably be linked to MW processing units in the future. The Cement Industry could enhance its environmental sustainability and achieve greater competitiveness and independence by integrating on-site production of eco-friendly fuels. This could be facilitated through the implementation of a microwave continuous unit to process biomass (Siddique et al., 2022) or to produce hydrogen (Dadsetan et al., 2023; Serra et al., 2020), the latter addressing concerns associated with hydrogen gas transportation. Furthermore, the on-site deployment of microwave units for carbon capture, utilization, and storage (CCUS), involving processes such as sintering fly ash samples containing unburned carbon and $CaCO_3$ (Kashimura et al., 2023), would align with circular economy principles. Although early CCUS implementation may result in increased cement costs, government incentives, such as tax credits for CO_2 injection or storage, are making carbon capture more financially viable (Agency, 2023b).

5. Conclusions

In line with our aim to advance Microwave Continuous Processing Technology and enhance system performance, this study presents a computational multi-physics model developed with the COMSOL software that replicates the microwave continuous processing of limestone. We investigated the impact of five different material fill-ratios on energy dynamics and assessed the energy efficiency of the system. Employing a coupled approach, our three-dimensional model solves Maxwell's equations alongside energy and species transport equations, providing comprehensive insights into the complex interactions within the microwave continuous reactor.

(i) The automatic control of both impedance and P_{MW} plays a pivotal role in maintaining numerical stability and preventing excessive energy consumption, while also maximizing microwave heating performance during the continuous processing of limestone.
(ii) Setting the adequate material velocity, adjusted to meet residence time requirements for material processing, and the reactor layout, deliberately designed to induce electric field variation along material's propagation direction and perpendicular wave propagation onto the bed plane, are primary project considerations for the *in situ* and volumetric dissipation of electromagnetic energy.
(iii) Filling mass flux ratios and material velocity are identified as primary project variables for optimizing system performance through low temperature deviations, that remained below 18% relative to the average temperature.
(iv) The gradual temperature transition along the material's propagation stems from non-symmetric heat transfer mechanisms, arising due to the coupling of heat transfer with electromagnetic waves across different mediums, and to the surplus energy absorption by the diffusive term in loads below 100%-fill.
(v) Eq. (14) describes the spatial occurrence of maximum values of material temperature and electric field intensity through the variation of the material dielectric loss with temperature.
(vi) The parametric study revealed the operational conditions capable of optimizing global efficiency, achieving maximum microwave efficiency of 75% for 80%-fill load and thermal efficiencies surpassing 90% for loads exceeding 50%-fill.

Microwave Continuous Processing Technology presents itself as a promising avenue for innovation in the Cement Industry, aligning well with the principles of circular economy advocated by EU regulations. This study highlights the importance of employing an effective design and implementing specific control measures that optimize the performance of the Microwave Continuous Processing Technology.

CRediT authorship contribution statement

Sofia N. Gonçalves: Writing – review & editing, Writing – original draft, Validation, Software, Methodology, Investigation, Conceptualization. **Duarte M.S. Albuquerque:** Writing – review & editing, Supervision, Resources, Project administration, Conceptualization. **José C.F. Pereira:** Writing – review & editing, Supervision, Resources, Funding acquisition.

Declaration of competing interest

The authors declare the following financial interests/personal relationships which may be considered as potential competing interests: Duarte M. S. Albuquerque and Jose C. F. Pereira reports financial support was provided by European Union Seventh Framework Programme. Sofia do Nascimento Goncalves reports article publishing charges and equipment, drugs, or supplies were provided by Foundation for Science and Technology (FCT) through IDMEC. If there are other authors, they declare that they have no known competing financial interests or personal relationships that could have appeared to influence the work reported in this paper.

Data availability

Data will be made available on request.

Declaration of Generative AI and AI-assisted technologies in the writing process

During the preparation of this work the author used chat GPT in order to improve the syntax of the text. After using this tool, the author reviewed and edited the content as needed and takes full responsibility for the content of the publication.

Acknowledgements

These results are contributions from the project DESTINY, which has received funding from the European Union's Horizon 2020 research and innovation programme under grant agreement n° 820783.

Institutional acknowledgements: The authors acknowledge Fundação para a Ciência e a Tecnologia (FCT), Portugal for its financial support via the projects LAETA Base Funding (DOI: 10.54499/UIDB/50022/2020) and LAETA Programatic Funding, Portugal (DOI: 10.54499/UIDP/50022/2020).

The authors are grateful to the anonymous reviewers for their insightful and constructive comments that allowed us to improve the article.

References

Agency, E.E., 2023a. Greenhouse gas emission intensity of electricity generation in Europe. URL https://www.eea.europa.eu/ims/greenhouse-gas-emission-intensity-of-1.

Agency, I.E., 2023b. Section 45Q credit for carbon oxide sequestration. URL https://www.iea.org/policies/4986-section-45q-credit-for-carbon-oxide-sequestration.

Agency, E.E., 2023c. Share of energy consumption from renewable sources in europe. URL https://www.eea.europa.eu/ims/share-of-energy-consumption-from.

Ahmed, A., 2016. Effect of load on the heating efficiency and temperature uniformity in multi-mode cavity applicators. J. Microw. Power Electromagn. Energy 50, 123–137. http://dx.doi.org/10.1080/08327823.2016.1190170.

Amini, A., Latifi, M., Chaouki, J., 2021. Electrification of materials processing via microwave irradiation: A review of mechanism and applications. Appl. Therm. Eng. 193, 117003. http://dx.doi.org/10.1016/j.applthermaleng.2021.117003.

Behrend, R., García-Baños, B., Uhlig, V., Krause, H., Catala-Civera, J.M., 2016. Dielectric characterization of raw materials at high temperatures. Ceram. Forum Int. 93, E63–E69.

Bergman, T.L., Lavine, A.S., Incropera, F.P., 2011. Fundamentals of heat and mass transfer.

Bermúdeza, J., Benerosob, D., Rey-Raapb, N., Arenillasb, A., Menéndez, J., 2015. Energy consumption estimation in the scaling-up of microwave heating processes. Chem. Eng. Process.: Process Intensif. 95, 1–8. http://dx.doi.org/10.1016/j.cep.2015.05.001.

Bobok, E. (Ed.), 1993. Chapter 3. Balance Equations. vol. 32, Elsevier, pp. 35–58.

Catalá-Civera, J.M., Canós, A.J., Plaza-González, P., Gutiérrez, J.D., García-Baños, B., Peñaranda-Foix, F.L., 2015. Dynamic measurement of dielectric properties of materials at high temperature during microwave heating in a dual mode cylindrical cavity. IEEE Trans. Microw. Theory Tech. 63, 2905–2914. http://dx.doi.org/10.1109/TMTT.2015.2453263.

Chen, X., Wang, Y., Liu, Z., Dong, Q., Zhao, X., 2022. Temperature analyses of porous asphalt mixture using steel slag aggregates heated by microwave through laboratory tests and numerical simulations. J. Clean. Prod. 338, 130614. http://dx.doi.org/10.1016/j.jclepro.2022.130614.

Choate, W.T., 2003. Energy and Emission Reduction Opportunities for the Cement Industry. Technical Report, BCS, Incorporated.

Csernyei, C., Straatman, A.G., 2016. Numerical modeling of a rotary cement kiln with improvements to shell cooling. Int. J. Heat Mass Transf. 102, 610–621. http://dx.doi.org/10.1016/j.ijheatmasstransfer.2016.06.058.

Curet, S., Rouaud, O., Boillereaux, L., 2008. Microwave tempering and heating in a single-mode cavity: Numerical and experimental investigations. Chem. Eng. Process. 47, 1656–1665. http://dx.doi.org/10.1016/j.cep.2007.09.011.

Dadsetan, M., Khan, M.F., Salakhi, M., Bobicki, E.R., Thomson, M.J., 2023. CO2-free hydrogen production via microwave-driven methane pyrolysis. Int. J. Hydrog. Energy 48, 14565–14576. http://dx.doi.org/10.1016/j.ijhydene.2022.12.353.

Das, A., Banik, B.K., 2021. Chapter 3 - modeling and interpreting microwave effects. In: Microwaves in Chemistry Applications. In: Advances in Green and Sustainable Chemistry, Elsevier, pp. 61–104. http://dx.doi.org/10.1016/B978-0-12-822895-1.00007-2.

Escardino, A., Garcia-Ten, J., Feliu, C., 2008. Kinetic study of calcite particle (powder) thermal decomposition: Part i. J. Eur. Ceram. Soc. 28, 3011–3020. http://dx.doi.org/10.1016/j.jeurceramsoc.2008.05.017.

Esquenazi, G., Allan, S.M., Shulman, H., 2011. Rapid limestone calcination using microwave assist technology. In: Proceedings ACEEE 2011 Summer Studies on Energy Efficiency in Industry.

European Commission and Directorate-General for Internal Market, Industry, Entrepreneurship and SMEs, 2018. Competitiveness of the European cement and lime sectors: final report. Technical Report, Publications Office, http://dx.doi.org/10.2873/300170.

Fall, M.L., Yakovlev, V., Sahi, C., Baranova, I., Bowers, J.G., Esquenazi, G., 2012. Energy Efficient Microwave Hybrid Processing of Lime for Cement, Steel, and Glass Industries. Ceralink Inc., http://dx.doi.org/10.2172/1034621.

Fennell, P., Driver, J., Bataille, C., Davis, S.J., 2022. Cement and steel — nine steps to net zero. Nature 603, 574–577. http://dx.doi.org/10.1038/d41586-022-00758-4.

García-Baños, B., Ognyanova Tsvetkova, E., Llorens-Vallés, G., Catalá-Civera, J., 2016. Microwave heating of powders at high temperature: effect of grain size and bulk density. In: 3rd Global Congress on Microwave Energy Applications. http://dx.doi.org/10.1021/op500064k.

Goyal, H., Chen, T.-Y., Chen, W., Vlachos, D.G., 2022. A review of microwave-assisted process intensified multiphase reactors. Chem. Eng. J. 430, 133183. http://dx.doi.org/10.1016/j.cej.2021.133183.

Griffiths, D.J., 2017. Introduction to electrodynamics. http://dx.doi.org/10.1017/9781108333511.

Hanks, R.W., 2003. Fluid dynamics (chemical engineering). Encyclopedia of Physical Science and Technology, third ed. Academic Press, pp. 45–70.

Henein, H., Brimacombe, J.K., Watkinson, A.P., 1983. Experimental study of transverse bed motion in rotary kilns. Metall. Trans. B 14, 191–205. http://dx.doi.org/10.1007/BF02661016.

Huang, Z., Goto, M., Hirose, Y., 2009. Improving sinterability of ceramics using hybrid microwave heating. J. Mater. Process. Technol. 209, 2446–2452. http://dx.doi.org/10.1016/j.jmatprotec.2008.05.037.

Huayu, Y., Yuhao, Z., Wenhua, G., Bowen, Y., Jianxin, Z., Hao, Z., Wei, C., Daming, F., 2021. Steam replacement strategy using microwave resonance: A future system for continuous-flow heating applications. Appl. Energy 283, 116300. http://dx.doi.org/10.1016/j.apenergy.2020.116300.

Juan, L., Shichang, S., Xing, C., Junhao, L., Rui, M., Rui, Z., Lin, F., 2021. In-depth exploration of the energy utilization and pyrolysis mechanism of advanced continuous microwave pyrolysis. Appl. Energy 292, 116941. http://dx.doi.org/10.1016/j.apenergy.2021.116941.

Jung, S., Kwak, J.H., Han, S.M., 2021. Guided-wavelength-controlled dynamic microwave heating in a near-cutoff waveguide. Appl. Therm. Eng. 188, 116630. http://dx.doi.org/10.1016/j.applthermaleng.2021.116630.

Kaewwichit, P., Junsomboon, J., Chakartnarodom, P., Tippayasam, C., Srichumpong, T., Thavorniti, P., Leonelli, C., Chaysuwan, D., 2016. Development of microwave-assisted sintering of Portland cement raw meal. J. Clean. Prod. 142, 1252–1258. http://dx.doi.org/10.1016/j.jclepro.2016.07.009.

Kashimura, K., Oshita, A., Miyata, T., Segawa, S., Yokawa, H., Tendo, K., Kurooka, K., 2023. Manufacturing carbon storage sintered body using microwave-selective and high-speed heating techniques. Sci. Rep. 13 (1), 5122. http://dx.doi.org/10.1038/s41598-023-32136-z.

Komarov, V.V., 2012. Dielectric and thermal properties of materials at microwave frequencies.

Kong, Y., Liu, S., Wang, P., 2021. Effects of microwave curing on the compressive strength development and hydration of cement-granulated blast furnace slag composite system. Constr. Build. Mater. 270, 121432. http://dx.doi.org/10.1016/j.conbuildmat.2020.121432.

Kopyt, P., Celuch, M., 2006. Coupled electromagnetic-thermodynamic simulations of microwave heating problems using the FDTD Algorithm. J. Microw. Power Electromagn. Energy 41, 18–29. http://dx.doi.org/10.1080/08327823.2006.11688568.

Li, Z., Zhang, X., Ma, G., Zheng, D., Xu, J., Xu, J., 2022. Effect of the Fe/Cr molar ratio and calcination temperature on the preparation of black ceramic pigment with stainless steel dust assisted by microwave processing. J. Clean. Prod. 372, 133751. http://dx.doi.org/10.1016/j.jclepro.2022.133751.

Lu, D., Jiang, X., Leng, Z., 2024. Sustainable microwave-heating healing asphalt concrete fabricated with waste microwave-sensitive fillers. J. Clean. Prod. 434, 140343. http://dx.doi.org/10.1016/j.jclepro.2023.140343.

Makul, N., Rattanadecho, P., Agrawal, D.K., 2014. Applications of microwave energy in cement and concrete – A review. Renew. Sustain. Energy Rev. 37, 715–733. http://dx.doi.org/10.1016/j.rser.2014.05.054.

Mastorakos, E., Massias, A., Tsakiroglou, C.D., Goussis, D.A., Burganos, V.N., Payatakes, A.C., 1999. CFD predictions for cement kilns including flame modelling, heat transfer and clinker chemistry. Appl. Math. Model. 23, 55–76. http://dx.doi.org/10.1016/S0307-904X(98)10053-7.

Mendes, J., 2017. Simulation of Cement Clinker Process by of Microwave Heating (Master's thesis). Instituto Superior Técnico.

Mimoso, R.M.C., Albuquerque, D.M.S., Pereira, J.M.C., Pereira, J.C.F., 2017. Simulation and control of continuous glass melting by microwave heating in a single-mode cavity with energy efficiency optimization. Int. J. Therm. Sci. 111, 175–187. http://dx.doi.org/10.1016/j.ijthermalsci.2016.08.015.

Modarresifar, F., Bingham, P.A., Jubb, G.A., 2016. Thermal conductivity of refractory glass fibres: A study of materials, standards and test methods. J. Therm. Anal. Calorim. 125, 35–44. http://dx.doi.org/10.1007/s10973-016-5367-0.

Morschhäuser, R., Krull, M., Kayser, C., Boberski, C., Bierbaum, R., Püschner, P.A., Glasnov, T.N., Kappe, C.O., 2012. Microwave-assisted continuous flow synthesis on industrial scale. Green Process. Synth. 1, 281–290. http://dx.doi.org/10.1515/gps-2012-0032.

Naqi, A., Jang, J.G., 2019. Recent progress in green cement technology utilizing low-carbon emission fuels and raw materials: A review. Sustainability 11, 537. http://dx.doi.org/10.3390/su11020537.

Ochoa George, P.A., Gutiérrez, A.S., Cogollos Martínez, J.B., Vandecasteele, C., 2010. Cleaner production in a small lime factory by means of process control. J. Clean. Prod. 18 (12), 1171–1176. http://dx.doi.org/10.1016/j.jclepro.2010.03.019.

Papargyris, D.A., Day, R.J., Nesbitt, A., Bakavos, D., 2008. Comparison of the mechanical and physical properties of a carbon fibre epoxy composite manufactured by resin transfer moulding using conventional and microwave heating. Compos. Sci. Technol. 68, 1854–1861. http://dx.doi.org/10.1016/j.compscitech.2008.01.010.

Patil, N.G., Benaskar, F., Rebrov, E.V., Meuldijk, J., Hulshof, L.A., Hessel, V., Schouten, J.C., 2014. Scale-up of microwave assisted flow synthesis by transient processing through monomode cavities in series. Org. Process Res. Dev. 18, 1400–1407. http://dx.doi.org/10.1021/op500064k.

Pérez-Maqueda, L.A., Sánchez-Jiménez, P.E., Criado, J.M., 2005. Kinetic analysis of solid-state reactions: Precision of the activation energy calculated by integral methods. Int. J. Chem. Kinet. 37, 658–666. http://dx.doi.org/10.1002/kin.20115.

Pozar, D.M., 2015. Microwave engineering. Microwave Engineering, fourth ed. John Wiley & Sons.

Qiao, X., Xie, X., 2016. The effect of electric field intensification at interparticle contacts in microwave sintering. Sci. Rep. 6, 32163. http://dx.doi.org/10.1038/srep32163.

Ramos, P.A.V., Albuquerque, D.M.S., Pereira, J.C.F., 2021. Numerical simulation and optimization of the ceramic pigments production process using microwave heating. Chemical Engineering and Processing - Process Intensification 169, 108567. http://dx.doi.org/10.1016/j.cep.2021.108567.

Reinosa, J., García-Baños, B., Catalá-Civera, J., Fernández, J., 2019. A step ahead on efficient microwave heating for kaolinite. Appl. Clay Sci. 168, 237–243. http://dx.doi.org/10.1016/j.clay.2018.11.001.

Ritchie, H., Roser, M., 2020. Energy. URL https://ourworldindata.org/energy.

Rossi, M., Rocco, V.M., 2014. External walls design: The role of periodic thermal transmittance and internal areal heat capacity. Energy Build. 68, 732–740. http://dx.doi.org/10.1016/j.enbuild.2012.07.049.

Roy, C.J., 2005. Review of code and solution verification procedures for computational simulation. J. Comput. Phys. 205, 131–156. http://dx.doi.org/10.1016/j.jcp.2004.10.036.

Scarlat, N., Prussi, M., Padella, M., 2022. Quantification of the carbon intensity of electricity produced and used in Europe. Appl. Energy 305, 117901. http://dx.doi.org/10.1016/j.apenergy.2021.117901.

Serra, J.M., Borrás-Morell, J.F., García-Baños, B., Balaguer, M., Plaza-González, P., Santos-Blasco, J., Catalán-Martínez, D., Navarrete, L., Catalá-Civera, J.M., 2020. Hydrogen production via microwave-induced water splitting at low temperature. Nat. Energy 5, 910–919. http://dx.doi.org/10.1038/s41560-020-00720-6.

Shah, Y.T., 2018. Thermal energy: Sources recovery and applications. http://dx.doi.org/10.1201/9781315305950.

Siddique, I.J., Salema, A.A., Antunes, E., Vinu, R., 2022. Technical challenges in scaling up the microwave technology for biomass processing. Renew. Sustain. Energy Rev. 153, http://dx.doi.org/10.1016/j.rser.2021.111767.

Sun, J., Wenlong, W., Yue, Q., 2016. Review on microwave-matter interaction fundamentals and efficient microwave-associated heating strategies. Materials (Basel) 9, http://dx.doi.org/10.3390/ma9040231.

Tokheim, L.A., Mathisen, A., Øi, L.E., Jayarathna, C., Eldrup, N., Gautestad, T., 2019. Combined calcination and CO2 capture in cement clinker production by use of electrical energy. In: Trondheim CO2 Capture, Transport and Storage Conference. Vol. 4, pp. 101–109.

Vaz, R.H., Pereira, J.M.C., Ervilha, A.R., Pereira, J.C.F., 2014. Simulation and uncertainty quantification in high temperature microwave heating. Appl. Therm. Eng. 70, 1025–1039. http://dx.doi.org/10.1016/j.applthermaleng.2014.06.005.

Vilchevskaya, E.N., Müller, W.H., 2021. Modeling of orientational polarization within the framework of extended micropolar theory. Contin. Mech. Thermodyn. 33, 1263–1279. http://dx.doi.org/10.1007/s00161-021-00972-x.

Voldsund, M., Gardarsdottir, S.O., De Lena, E., Pérez-Calvo, J.-F., Jamali, A., Berstad, D., Fu, C., Romano, M., Roussanaly, S., Anantharaman, R., Hoppe, H., Sutter, D., Mazzotti, M., Gazzani, M., Cinti, G., Jordal, K., 2019. Comparison of technologies for CO2 capture from cement production - Part 1: Technical evaluation. Energies 12, 559. http://dx.doi.org/10.3390/en12030559.

Vyas, S.K., Maurya, S., Verma, R.K., Singh, V.P., 2015. Synthesis and simulation studies of a 10-kW 2.45-GHz CW magnetron. IEEE Trans. Plasma Sci. 43, 3615–3619. http://dx.doi.org/10.1109/TPS.2015.2475182.

Wojtacha-Rychter, K., Kucharski, P., Smolinski, A., 2021. Conventional and alternative sources of thermal energy in the production of cement - An impact on CO2 emission. Energies 14, 1539. http://dx.doi.org/10.3390/en14061539.

Yilmaz, M., Comakli, O., Yapici, S., Sara, O., 2005. Performance evaluation criteria for heat exchangers based on first law analysis. J. Enhanc. Heat Transf. 12, 121–158. http://dx.doi.org/10.1016/S1164-0235(01)00034-6.

Zaki, N.A.M., Alwi, H., Hashib, S.A., Ibrahim, U.K., Jai, J., 2023. Microwave drying characteristics and quality of Ananas comosus peel, core and pulp. Mater. Today: Proc. 87, 8–12. http://dx.doi.org/10.1016/j.matpr.2023.01.367.

Zhou, C., Zhang, Y., Xing, X., Zhang, T., Siyal, A.A., Liu, Y., Dai, J., Qu, J., Liu, C., Yao, B., Chao, L., Chen, L., Chen, Y., Wang, J., Dong, J., Wang, L., 2023. Comparative study of continuous and batch microwave-assisted pyrolysis of waste printed circuit boards: product characteristic, bromine transformation, and energy efficiency assessment. J. Clean. Prod. 421, 138546. http://dx.doi.org/10.1016/j.jclepro.2023.138546.

Zhu, J., Li, X., Yang, Z., Zhou, J., Wang, H., 2022. Drying characteristics of oil shale under microwave heating based on a fully coupled three-dimensional electromagnetic-thermal-multiphase transport model. Fuel 308, 121942. http://dx.doi.org/10.1016/j.fuel.2021.121942.